IEEE Access
Multidisciplinary | Rapid Review | Open Access Journal

Received 7 November 2024, accepted 10 December 2024, date of publication 18 December 2024,
date of current version 27 December 2024.

Digital Object Identifier 10.1109/ACCESS.2024.3517707

RESEARCH ARTICLE

A Multi-Frequency Iterative Method for Reconstruction of Rough Surfaces Separating Two Penetrable Media

AHMET SEFER[1,2], (Member, IEEE), ALI YAPAR[3], AND HAKAN BAGCI[1], (Senior Member, IEEE)

[1]Electrical and Computer Engineering (ECE) Program, Computer, Electrical, and Mathematical Science and Engineering (CEMSE) Division, King Abdullah University of Science and Technology (KAUST), Thuwal 23955, Saudi Arabia
[2]Department of Electrical and Electronics Engineering, Fevziye Schools Foundation, Isik University, 34882 Istanbul, Türkiye
[3]Department of Electronics and Communications Engineering, Istanbul Technical University, 34469 Istanbul, Türkiye

Corresponding author: Ahmet Sefer (ahmet.sefer@kaust.edu.sa)

ABSTRACT A numerical scheme that uses multi-frequency Newton iterations to reconstruct a rough surface profile between two dielectric media is proposed. At each frequency sample, the scheme employs Newton iterations to solve the nonlinear inverse scattering problem. At every iteration, the Newton step is computed by solving a linear system that involves the Frechet derivative of the integral operator, which represents the scattered fields, and the difference between these fields and the measurements. This linear system is regularized using the Tikhonov method. The multi-frequency data is accounted for in a recursive manner. More specifically, the profile reconstructed at a given frequency is used as an initial guess for the iterations at the next frequency. The effectiveness of the proposed method is validated through numerical examples, which demonstrate its ability to accurately reconstruct surface profiles even in the presence of measurement noise. The results also show the superiority of the multi-frequency approach over single-frequency reconstructions, particularly in terms of handling surfaces with sharp variations.

INDEX TERMS Inverse scattering problems, multi-frequency algorithm, Newton iterative method, rough surface reconstruction, surface integral equations.

I. INTRODUCTION

Reconstruction of inaccessible rough surfaces from measured scattered electromagnetic fields is a subject of significant interest in various engineering disciplines, such as remote sensing [1], [2], [3], [4], optical system measurement [5], subsurface imaging [6], [7], [8], ultrasonic applications like wall-thickness measurement [9], damage detection [10], [11], and nondestructive testing [12], [13], [14]. This reconstruction requires solving an inverse problem where the scattered fields are represented as convolutions of the Green functions of the background media with the fields on the unknown surface profile [15]. This inverse problem is inherently ill-posed due to the contamination of the measured scattered field data by noise and the ''smoothing'' effect introduced by the convolution integrals [16], [17]. Furthermore, the scattered fields are nonlinear functions of the unknown surface profile [16], [17]. The ill-posedness and nonlinearity of the inverse problem make the reconstruction of the surface profile a highly challenging task.

Among the methods that are developed to address these challenges, semi-analytical approaches that rely on Kirchhoff [18], small-perturbation [19] and Rytov [20] approximations, or low-order expansion of fields [21] and fully numerical approaches that rely on reverse time migration (RTM) [22] can be considered ''direct'' solution techniques, i.e., they are non-iterative.

The other group of solution techniques [23], [24], [25], [26], [27], [28], [29], [30], [31], [32] minimize the error between the measured scattered fields and the scattered

The associate editor coordinating the review of this manuscript and approving it for publication was Wei E. I. Sha.

fields of a predicted profile that is updated iteratively to ''linearize'' the inverse problem. Often, the regularization is applied at every iteration to alleviate the ill-posedness. The method described in [23], [24], and [25] iteratively updates the derivative of the field on the surface and the surface profile that are coupled via the convolution integral and a simple relationship that is obtained under the assumption of grazing incident field. In [26] and [27], Landweber iterations are used for linearization and regularization of the reconstruction of periodic gratings and rough surfaces from phaseless data, respectively. In contrast, the method proposed in [28] inverts the full scattered fields (with phase and amplitude) to reconstruct rough surfaces separating two dielectric media. A Newton method is used for linearization while the regularization at every Newton iteration is carried out by applying the truncated conjugate gradient method to the normal equation of the Newton update.

Similarly, in [29], a Newton method is used for the reconstruction of rough surfaces separating two dielectric media from full scattered-field measurements. At every iteration, a linear system in the Newton step of the unknown profile is constructed. This linear system involves the Frechet derivative of the convolution operator, which is used in the representation of the fields scattered from the profile updated at that iteration and the difference between these scattered fields and the measurements. To alleviate the ill-posedness of this linear system, Tikhonov regularization is applied before it is solved for the Newton step. In [30], a similar iterative method is developed for the reconstruction of sound-soft rough surfaces of acoustics. In [31] and [32], the Newton method in [29] is extended for reconstruction using phaseless data and reconstruction of impedance surfaces, respectively.

The performance of these iterative approaches can be improved using multi-frequency/multi-resolution based techniques since the use of multi-frequency/scale data alleviates the effects of ill-conditioning, reduces the occurrence of false solutions, and helps to avoid local minima of the minimization problem by mitigating the effects of nonlinearity [33], [34], [35]. Indeed, these techniques have been used to improve solutions of inverse scattering problems in a range applications changing from ground penetrating radar (GPR) [8], [36] to microwave imaging [37], non-destructive testing [38] and diffraction tomography [39]. In [8], a multi-scale and multi-frequency approach is used to iteratively reconstruct the scatterer profile from time-domain GPR data. In [36], a multi-frequency contrast source imaging (CSI) method that exploits multi-view wide band GPR data is developed to reconstruct pixel-sparse subsurface objects. In [37], a recursive multi-scale approach is used in conjunction with the contradiction integral equation to retrieve the unknown relative permittivity of a complex-shaped strong scatterer.

In this work, the Tikhonov-regularized Newton iterative scheme, which is proposed in [29] to reconstruct a rough surface separating two dielectric media from full scattered-field measurements, is extended to account for multi-frequency data. This extension represents the primary contribution of the study. Additionally, the advantages of using the resulting multi-frequency Newton iterations are clearly demonstrated. More specifically:

1) The use of multi-frequency data improves the accuracy and the resolution of the reconstruction as demonstrated by the numerical examples in Section III. For instance, for the example in Section III-D, the single-frequency Newton iterations fail to capture sharp surface features, whereas the proposed multi-frequency method reconstructs a profile much closer to the actual surface.
2) The multi-frequency data are incorporated iteratively, with the reconstruction at each frequency serving as an initial guess for the Newton iterations at the next frequency. This approach mitigates the nonlinearity of the inverse problem, leading to more robust, stable, and efficient reconstructions. For several examples in Section III, the single-frequency Newton iterations fail to converge while the multi-frequency method reconstructs the surface accurately. For the second example in Section III-F, the multi-frequency Newton method reconstructs the surface faster and with a higher level of accuracy than its single-frequency version.
3) In addition to these two main points, an extensive set of examples are provided to demonstrate the robustness and accuracy of multi-frequency reconstruction across various noise levels, different numbers of measurements and frequency sampling rates. These results have archival value and can serve as a reference for validation of other approaches.

The rest of the paper is organized as follows: Section II expounds on the formulation underlying the proposed multi-frequency Newton iterations. Section II-A describes the set-up of the problem. Section II-B provides the formulation for the forward scattering problem in terms of integral equations. Section II-C describes the linearization of the nonlinear inverse scattering problem via Newton iterations and its regularization via the Tikhonov method. Section II-D provides the final form of the proposed method in the form of an algorithm and describes how multi-frequency data is accounted for. Comprehensive numerical results are provided in Section III to demonstrate the applicability, accuracy, and efficiency of the proposed multi-frequency Newton iterations. Finally, conclusions follow in Section IV.

II. FORMULATION

A. PROBLEM SETUP

Fig. 1 describes the two-dimensional (2D) scattering problem involving a rough surface that separates two penetrable media. It is assumed that Ω_1 is lossless and Ω_2 is lossy with finite conductivity. The permeability, the permittivity, and the wavenumber in Ω_1 are denoted by μ_1, ε_1, and k_1 and the permeability, the permittivity, the conductivity, and the wavenumber in Ω_2 are denoted by μ_2, ε_2, σ_2, and k_2, respectively. The rough surface separating Ω_1 and

Ω_2 is denoted by Γ and expressed using a continuous height function $y = s(x)$, $L/2 \geq x \geq -L/2$. Since Γ is assumed to be of finite length, a "traditional" plane wave excitation gives rise to diffraction on the edges of the surface. Therefore, a plane wave with the Thorsos taper is used as excitation [40]. Assuming that the plane wave originates in Ω_1, the incident field is expressed using

$$u^{\text{inc}}(\mathbf{r}) = e^{ik_1\hat{\mathbf{k}}^{\text{inc}}\cdot\mathbf{r}} e^{-\left(\frac{x+y\tan\theta^{\text{inc}}}{g}\right)^2} e^{\mathrm{i}\left(\xi(\mathbf{r})k_1\hat{\mathbf{k}}^{\text{inc}}\cdot\mathbf{r}\right)}. \tag{1}$$

In (1), $\mathbf{r} = (x, y)$ is the location vector in the 2D space, $\hat{\mathbf{k}}^{\text{inc}} = (\sin\theta^{\text{inc}}, -\cos\theta^{\text{inc}})$ is the direction of propagation, θ^{inc} is the angle of incidence, and the second and the third exponents are the decay factor and the correction term associated with the Thorsos taper, respectively. The decay factor is defined such that $u^{\text{inc}}(\mathbf{r})$ decays in the direction perpendicular to $\hat{\mathbf{k}}^{\text{inc}}$. The correction term, where the function $\xi(\mathbf{r})$ is defined as

$$\xi(\mathbf{r}) = \left[\left(\frac{2\left(x + y\tan\theta^{\text{inc}}\right)^2}{g^2}\right) - 1\right] \frac{1}{\left(k_1 g\cos\theta^{\text{inc}}\right)^2} \tag{2}$$

ensures that $u^{\text{inc}}(\mathbf{r})$ satisfies the scalar Helmholtz equation to order $1/(k_1 g\cos\theta^{\text{inc}})^3$ [15]. In (1) and (2), the parameter g controls the width of the taper.

B. FORWARD SCATTERING PROBLEM

Let $u_1(\mathbf{r})$ and $u_2(\mathbf{r})$ represent the total field in Ω_1 and Ω_2, respectively. Using equivalence and extinction theorems [41], one can obtain the integral representations of $u_1(\mathbf{r})$ and $u_2(\mathbf{r})$ as

$$u_1(\mathbf{r}) = u^{\text{inc}}(\mathbf{r}) + \int_\Gamma \Big[K_1(\mathbf{r},\mathbf{r}')u_1(\mathbf{r}') - G_1(\mathbf{r},\mathbf{r}')v_1(\mathbf{r}')\Big]dl' \quad \mathbf{r}\in\Omega_1 \tag{3a}$$

$$u_2(\mathbf{r}) = -\int_\Gamma \Big[K_2(\mathbf{r},\mathbf{r}')u_2(\mathbf{r}') - G_2(\mathbf{r},\mathbf{r}')v_2(\mathbf{r}')\Big]dl' \quad \mathbf{r}\in\Omega_2. \tag{3b}$$

Here, $G_m(\mathbf{r},\mathbf{r}') = (\mathrm{i}/4)H_0^{(1)}(k_m|\mathbf{r}-\mathbf{r}'|)$, $m \in \{1,2\}$ is the fundamental solution (Green function) of the scalar Helmholtz equation in 2D unbounded space with wavenumber k_m, $H_0^{(1)}(.)$ is the Hankel function of the first kind and order zero, and $K_m(\mathbf{r},\mathbf{r}') = \hat{\mathbf{n}}(\mathbf{r}')\cdot\nabla' G_m(\mathbf{r},\mathbf{r}')$, $\mathbf{r}' \in \Gamma$ is the derivative of $G_m(\mathbf{r},\mathbf{r}')$ with respect to surface unit normal vector $\hat{\mathbf{n}}(\mathbf{r}')$. Note that $\hat{\mathbf{n}}(\mathbf{r})$, $\mathbf{r}\in\Gamma$ points from Ω_2 to Ω_1. Similarly, $v_m(\mathbf{r}) = \hat{\mathbf{n}}(\mathbf{r})\cdot\nabla u_m(\mathbf{r})$, $\mathbf{r}\in\Gamma$ is the derivative of $u_m(\mathbf{r})$ with respect to $\hat{\mathbf{n}}(\mathbf{r})$. The fields $u_1(\mathbf{r})$ and $u_2(\mathbf{r})$ and their normal derivatives $v_1(\mathbf{r})$ and $v_2(\mathbf{r})$ are continuous on Γ:

$$u_1(\mathbf{r}) = u_2(\mathbf{r}) = u(\mathbf{r}),\ \mathbf{r}\in\Gamma \tag{4a}$$

$$v_1(\mathbf{r}) = v_2(\mathbf{r}) = v(\mathbf{r}),\ \mathbf{r}\in\Gamma. \tag{4b}$$

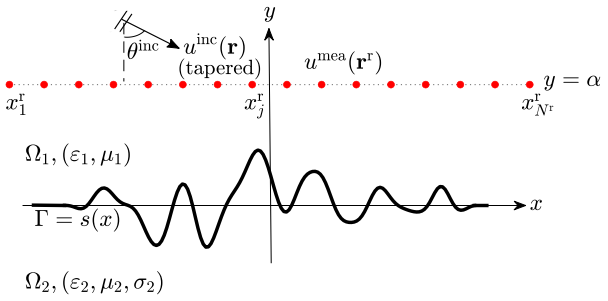

FIGURE 1. 2D scattering problem involving a rough surface separating two dielectric media.

Inserting (4a) and (4b) into (3a) and (3b) and letting $\mathbf{r}\to\Gamma$ yield a coupled system of two integral equations:

$$\frac{1}{2}u(\mathbf{r}) - \fint_\Gamma K_1(\mathbf{r},\mathbf{r}')u(\mathbf{r}')\,dl' + \int_\Gamma G_1(\mathbf{r},\mathbf{r}')v(\mathbf{r}')\,dl' = u^{\text{inc}}(\mathbf{r}),\ \mathbf{r}\in\Gamma \tag{5a}$$

$$\frac{1}{2}u(\mathbf{r}) + \fint_\Gamma K_2(\mathbf{r},\mathbf{r}')u(\mathbf{r}')\,dl' - \int_\Gamma G_2(\mathbf{r},\mathbf{r}')v(\mathbf{r}')dl' = 0,\ \mathbf{r}\in\Gamma \tag{5b}$$

Symbol "$-$" shown on the first integrals of (5a) and (5b) means that these integrals are to be evaluated in the Cauchy principle value sense [42].

Equations (5a)-(5b) define the forward scattering problem. For a given $\Gamma = s(x)$ and a given $u^{\text{inc}}(\mathbf{r})$, they are numerically solved for $u(\mathbf{r})$ and $v(\mathbf{r})$, $\mathbf{r}\in\Gamma$ as described next. For numerical solution, the finite domain $-L/2 \leq x \leq L/2$, is divided into N^{s} number of equal segments of width w. Midpoints of these segments are represented by x_i^{s}, $i = 1, 2, \ldots, N^{\text{s}}$. Unknowns $u(x, s(x))$ and $v(x, s(x))$ are expanded in terms of basis functions as

$$u(x, s(x)) = \sum_{i=1}^{N^{\text{s}}} \bar{u}_i f_i(x) \tag{6a}$$

$$v(x, s(x)) = \sum_{i=1}^{N^{\text{s}}} \bar{v}_i f_i(x). \tag{6b}$$

Here, $f_i(x)$ are the pulse basis functions (see Appendix A), and $\bar{u}$ and $\bar{v}$ are the vectors that collect the unknown coefficients associated with these basis functions. Inserting expansions (6a) and (6b) into (5a) and (5b) and point testing the resulting equations at $x_j^{\text{s}}, j = 1, 2, \ldots, N^{\text{s}}$ yields a matrix equation as

$$\underbrace{\begin{bmatrix}\bar{Z}^{11} & \bar{Z}^{12}\\ \bar{Z}^{21} & \bar{Z}^{22}\end{bmatrix}}_{\bar{Z}}\begin{bmatrix}\bar{u}\\ \bar{v}\end{bmatrix} = \begin{bmatrix}\bar{u}^{\text{inc}}\\ \bar{0}\end{bmatrix}. \tag{7}$$

Here, $\bar{u}^{\text{inc}}$ is the vector of the tested incident field, and $\bar{Z}$ is the impedance matrix. Their elements are detailed in Appendix A. In this work, the matrix equation (7) is solved by directly inverting the impedance matrix but for large N^{s}, one

can use an iterative method together with well-established acceleration techniques to reduce the computation time and the memory requirement [43], [44], [45], [46], [47].

C. INVERSE SCATTERING PROBLEM

The scattered field $u^{\text{sca}}(\mathbf{r})$ in Ω_1 is expressed in terms of $u(\mathbf{r}')$ and $v(\mathbf{r}')$ using (3a) as

$$u^{\text{sca}}(\mathbf{r}) = u_1(\mathbf{r}) - u^{\text{inc}}(\mathbf{r}) = \int_\Gamma \Big[K_1(\mathbf{r},\mathbf{r}')u(\mathbf{r}') - G_1(\mathbf{r},\mathbf{r}')v(\mathbf{r}')\Big]dl', \mathbf{r}\in\Omega_1. \tag{8}$$

Equation (8) can be written in a more compact form as

$$u^{\text{sca}}(\mathbf{r}) = \mathcal{D}[s,u,v](\mathbf{r}) \tag{9}$$

where the operator $\mathcal{D}[s,u,v](\mathbf{r})$ is given by

$$\mathcal{D}[s,u,v](\mathbf{r}) = \int_{\Gamma(s)} \Big[K_1(\mathbf{r},\mathbf{r}')u(\mathbf{r}') - G_1(\mathbf{r},\mathbf{r}')v(\mathbf{r}')\Big]dl'. \tag{10}$$

For the inverse scattering problem, the field scattered from $\Gamma = s(x)$ under excitation by $u^{\text{inc}}(\mathbf{r})$ is measured at N^{r} number of points located in Ω_1. The locations of these points are represented by $\mathbf{r}^{\text{r}} = (x_j^{\text{r}}, \alpha)$, $j = 1, 2, \ldots, N^{\text{r}}$ (see Fig. 1). This measured scattered field is represented by $u^{\text{mea}}(\mathbf{r}^{\text{r}})$. Then, the inverse scattering problem is defined as reconstructing the unknown $s(x)$ from $u^{\text{mea}}(\mathbf{r}^{\text{r}})$, i.e., it calls for solving

$$\mathcal{D}[s,u,v](x_j^{\text{r}},\alpha) = u^{\text{mea}}(x_j^{\text{r}},\alpha),\ j = 1,2,\ldots,N^{\text{r}} \tag{11}$$

for $s(x)$. Equation (11) is nonlinear in $s(x)$, $u(\mathbf{r})$, and $v(\mathbf{r})$ [this can be seen from (5a)-(5b) and (10)-(9)]. Therefore, its numerical solution calls for linearization [16]. In this work, this is done using a Newton iterative method [29]. Let n represent the Newton iteration number, and superscript "(n)" attach to a variable in braces mean that that variable is updated/computed at iteration n. The resulting Newton update equation reads:

$$\mathcal{D}'\Big[\{s\}^{(n)},\{u\}^{(n)},\{v\}^{(n)}\Big](x_j^{\text{r}},\alpha)\{\delta s(x)\}^{(n)} = u^{\text{mea}}(x_j^{\text{r}},\alpha) - \mathcal{D}\Big[\{s\}^{(n)},\{u\}^{(n)},\{v\}^{(n)}\Big](x_j^{\text{r}},\alpha),\ j = 1,2,\ldots,N^{\text{r}} \tag{12}$$

where $\delta s(x)$ is the unknown Newton step and $\mathcal{D}'[s,u,v](\mathbf{r})$ is the Frechet derivative of the operator $\mathcal{D}[s,u,v](\mathbf{r})$ with respect $s(x)$ [29]. Equation (12) is numerically solved for $\{\delta s(x)\}^{(n)}$. To facilitate the numerical solution, $\{s(x)\}^{(n)}$ and $\{\delta s(x)\}^{(n)}$ are expanded in terms of (entire-domain) basis functions as

$$\{s(x)\}^{(n)} = \sum_{i=1}^{N^{\text{p}}} \{\bar{s}_i\}^{(n)}\phi_i(x) \tag{13a}$$

$$\{\delta s(x)\}^{(n)} = \sum_{i=1}^{N^{\text{p}}} \{\bar{d}_i\}^{(n)}\phi_i(x)z \tag{13b}$$

Here, $\phi_i(x)$ are the spline-type basis functions (see Appendix B), and $\bar{s}$ and $\bar{d}$ are the vectors that collect the coefficients associated with these basis functions. To compute the unknown vector $\bar{d}$, first, (13a) is used in the forward problem with $\{s(x)\}^{(n)}$ as the input, then the forward problem matrix equation (7) is solved for $\{\bar{u}\}^{(n)}$ and $\{\bar{v}\}^{(n)}$. $\{u(x,s(x))\}^{(n)}$ and $\{v(x,s(x))\}^{(n)}$ approximated using (6a) and (6a), and $\{s(x)\}^{(n)}$ and $\{\delta s(x)\}^{(n)}$ approximated using (13a) and (13b) are inserted into (12). This yields a matrix equation as

$$\{\bar{C}\}^{(n)}\{\bar{d}\}^{(n)} = \{\bar{u}^{\text{mea}}\}^{(n)} - \{\bar{u}^{\text{sca}}\}^{(n)}. \tag{14}$$

Here, $\bar{u}^{\text{mea}}$ is the vector that collects the measured scattered field samples, $\bar{u}^{\text{sca}}$ is the vector that collects the samples of the fields scattered from $s(x)$ being reconstructed, and $\bar{C}$ is the matrix that represents the discretized Frechet derivative operator. Their elements are detailed in Appendix B.

$$(\{\bar{C}^H\}^{(n)}\{\bar{C}\}^{(n)} + \tau\bar{I})\{\bar{d}\}^{(n)} = \{\bar{C}^H\}^{(n)}(\{\bar{u}^{\text{mea}}\}^{(n)} - \{\bar{u}^{\text{sca}}\}^{(n)}). \tag{15}$$

Here, $\bar{C}^H$ is the Hermitian transpose of $\bar{C}$, $\bar{I}$ is the identity matrix, and τ is the regularization parameter that satisfies $0 < \tau < 1$. In this work, the matrix equation (15) is solved by directly inverting the matrix $(\{\bar{C}^H\}^{(n)}\{\bar{C}\}^{(n)} + \tau\bar{I})$. Equation (15) is the final discretized form of the Newton update equation that is solved for $\{\bar{d}\}^{(n)}$ at iteration n. The next step at iteration n is to update $\{s(x)\}^{(n+1)}$ using

$$\{s(x)\}^{(n+1)} = \{s(x)\}^{(n)} + \{\delta s(x)\}^{(n)}. \tag{16}$$

Equation (16) can be expressed in terms of the expansion coefficients $\{\bar{s}\}^{(n)}$ and $\{\bar{d}\}^{(n)}$ using (13a) and (13b)

$$\{\bar{s}\}^{(n+1)} = \{\bar{s}\}^{(n)} + \{\bar{d}\}^{(n)}. \tag{17}$$

Newton iterations are terminated when convergence in reconstruction is achieved, i.e., when the condition

$$\Big\|\{s(x)\}^{(n+1)} - \{s(x)\}^{(n)}\Big\|_2 = \Big\|\{\delta s(x)\}^{n}\Big\|_2 \le \xi \tag{18}$$

is satisfied. Here, ξ is a user-defined threshold. Condition (18) can be expressed in terms of the expansion coefficients $\{\bar{s}\}^{(n)}$ and $\{\bar{d}\}^{(n)}$

$$\Big\|\{\bar{s}\}^{(n+1)} - \{\bar{s}\}^{(n)}\Big\|_2 = \Big\|\{\bar{d}\}^{n}\Big\|_2 \le \tilde{\xi}, \tag{19}$$

where, similarly, $\tilde{\xi}$ is a user-defined threshold.

D. MULTI-FREQUENCY NEWTON ITERATIONS

As briefly discussed in Section I, multi-frequency data can be included in the iterative reconstruction process described in Section II-C to increase its stability and accuracy [33], [34], [35]. Assume that the scattered field measurements are taken at N^{f} number of frequency samples and let these samples be represented by $f_{(m)}$, $m = 1, 2, \ldots, N^{\text{f}}$. Then, the inverse scattering problem described by (11) is updated as

$$\mathcal{D}_{(m)}[s,u_{(m)},v_{(m)}](x_j^{\text{r}},\alpha) = u_{(m)}^{\text{mea}}(x_j^{\text{r}},\alpha)\quad j = 1,2,\ldots,N^{\text{r}}, m = 1,2,\ldots,N^{\text{f}}. \tag{20}$$

In (20) and the rest of the text, subscript "(m)" attached to a variable means that that variable is updated/computed at frequency $f_{(m)}$. To solve the inverse scattering problem (20), the Newton method briefly described in Section II-C and detailed in [29] is adopted to account for the multi-frequency data. The resulting multi-frequency Newton iterative method reads:

0 : collect $\bar{u}^{\text{mea}}_{(m)}$, $m = 1, 2, \ldots, N^{\text{f}}$ and initialize $\{\bar{s}_{(1)}\}^{(1)}$
1 : for $m = 1, 2, \ldots, N^{\text{f}}$
2.1 : for $n = 1, 2, \ldots$
2.1.1 : construct $s_{(m)}(x)$ using $\{\bar{s}_{(m)}\}^{(n)}$ in (13a)
2.1.2 : discretize $s_{(m)}(x)$ using $w_{(m)}$
2.1.3 : compute $\{\bar{Z}_{(m)}\}^{(n)}$, $\bar{u}^{\text{inc}}_{(m)}$
2.1.4 : solve (7) for $\{\bar{u}_{(m)}\}^{(n)}$, $\{\bar{v}_{(m)}\}^{(n)}$
2.1.5 : compute $\{\bar{C}_{(m)}\}^{(n)}$, $\{\bar{u}^{\text{sca}}_{(m)}\}^{(n)}$
2.1.6 : solve (15) for $\{\bar{d}_{(m)}\}^{(n)}$
2.1.7 : update $\{\bar{s}_{(m)}\}^{(n+1)} = \{\bar{s}_{(m)}\}^{(n)} + \{\bar{d}_{(m)}\}^{(n)}$
2.1.8 : check $\|\{\bar{d}_{(m)}\}^{(n)}\|_2 \leq \tilde{\xi}$
2.1.8.a : no : continue Newton iterations at $f_{(m)}$
2.1.8.b : yes : terminate Newton iterations at $f_{(m)}$
update $\{\bar{s}_{(m+1)}\}^{(1)} = \{\bar{s}_{(m)}\}^{(n+1)}$

Several comments about the above algorithm are in order: At Step 0, $\{\bar{s}_{(1)}\}^{(1)}$ is initialized to zero, i.e., $\{\bar{s}_{(1)}\}^{(1)} = \bar{0}$ which means via (13a) that the starting point of the iterations is a flat surface at $y = 0$. At Step 2.1.2, the discretization segment size $w_{(m)}$ is selected based on the spatial variations of the fields at frequency $f_{(m)}$. These are determined by the real and/or imaginary parts of the wavenumbers $k_{1,(m)}$ and $k_{2,(m)}$. Note that as $f_{(m)}$ increases $w_{(m)}$ decreases and the number of segments used in the discretization of the forward scattering problem $N^{\text{s}}_{(m)} = L/w_{(m)}$ increases. At Step 2.1.8, the convergence of the Newton iterations $f_{(m)}$ is checked. If the iterations converge (i.e., $\|\{\delta s_{(m)}(x)\}^{(n)}\|_2$ is small enough), the algorithm moves to $f_{(m+1)}$ and sets the initial guess for the Newton iterations at $f_{(m+1)}$ to the reconstruction converged at frequency $f_{(m)}$ (as shown in the second row of Step 2.1.8.b). The steps of the algorithm described above are illustrated in the flowchart in Fig. 2 for added clarity.

III. NUMERICAL RESULTS

In this section, numerical examples are presented to demonstrate the effectiveness of the multi-frequency Newton iterations. Let $s^{\text{ref}}(x)$ represent the actual surface profile in these numerical examples. $s^{\text{ref}}(x)$ is generated using the stationary random Gaussian process as described in [15], [40]. Two user-defined parameters determine the shape of $s^{\text{ref}}(x)$: ℓ that denotes the correlation length and h that denotes the standard deviation of the surface height. $s^{\text{ref}}(x)$ is defined in $-L/2 \leq x \leq L/2$, where $L = 16\,\text{m}$. In addition, tapered cosine windows are implemented on the surface to guarantee local roughness. This is done using the MATLAB built-in tukeywin(L, r) function, where $r = 25\,\text{cm}$ is the cosine fraction.

To generate $\bar{u}^{\text{mea}}$, first, the fields scattered from $s^{\text{ref}}(x)$ are computed by solving the forward scattering problem, and these fields are synthetically contaminated by noise using

$$\bar{u}^{\text{mea}}_j = \bar{u}^{\text{ref}}_j + |\bar{u}^{\text{ref}}_j| A_{\text{n}} e^{\text{i}2\pi P_{\text{n}}}, \; j = 1, 2, \ldots, N^{\text{r}}. \tag{21}$$

Here, A_{n} represents the noise level and P_{n} is a random number uniformly distributed in the range $[0,\ 1]$.

For all examples considered here, the permittivity and the permeability in Ω_1 and Ω_2 are $\varepsilon_1 = \varepsilon_0$ and $\mu_1 = \mu_0$ and $\varepsilon_2 = 4\varepsilon_0$ and $\mu_2 = \mu_0$, respectively. Here, ε_0 and μ_0 are the permittivity and the permeability in free space. The conductivity in Ω_2 is $\sigma_2 = 10^{-5}\,\text{S/m}$. For excitation, the angle of incidence $\theta^{\text{inc}} = 0°$ and the taper parameter $g = L/2$. The measurements are taken at points $\mathbf{r}^{\text{r}} = (x^{\text{r}}_j, \alpha)$, $j = 1, 2, \ldots, N^{\text{r}}$, where $\alpha = 4.25\,\text{m}$ and $x^{\text{r}}_j \in [x^{\text{r}}_{\text{sta}} : \Delta x^{\text{r}} : x^{\text{r}}_{\text{end}}]$ with $x^{\text{r}}_{\text{sta}} = -10\,\text{m}$ and $x^{\text{r}}_{\text{end}} = 10\,\text{m}$. The samples of frequency of operation $f_{(m)}$, $m = 1, 2, \ldots, N^{\text{f}}$ are in range $f_{(m)} \in [f_{\text{sta}} : \Delta f : f_{\text{end}}]$.

For all examples, the segment width used in the discretization of the forward scattering problem is $w_{(m)} = 2\pi/(10|k_{2,(m)}|)$, where $k_{2,(m)}$ is the wavenumber in Ω_2 at frequency $f_{(m)}$, the order of the spline basis functions is $p = 3$, the Newton iterations are terminated using threshold $\xi = 5 \times 10^{-3}$, and the Tikhonov regularization parameter $\tau = 0.75 \times 10^{-5}$.

The accuracy of the reconstruction is measured using

$$err_{(m)} = \sqrt{\frac{\sum_{i=1}^{N^{\text{s}}_{(m)}} \left[s^{(N)}_{(m)}(x^{\text{s}}_{i,(m)}) - s^{\text{ref}}(x^{\text{s}}_{i,(m)}) \right]^2}{\sum_{i=1}^{N^{\text{s}}_{(m)}} \left[s^{\text{ref}}(x^{\text{s}}_{i,(m)}) \right]^2}} \tag{22}$$

where $s^{(N)}_{(m)}(x)$ is the reconstruction at the last Newton iteration (N) at frequency $f_{(m)}$.

A. CONVERGENCE

The first example demonstrates the convergence of error in the reconstruction over frequency. For the first example, $s^{\text{ref}}(x)$ is generated with $\ell = 0.7\,\text{m}$ and $h = 0.07\,\text{m}$. The simulation parameters are $A_{\text{n}} = 5\%$, $f_{\text{sta}} = 325\,\text{MHz}$, $f_{\text{end}} = 900\,\text{MHz}$, $\Delta f = 25\,\text{MHz}$, $\Delta x^{\text{r}} = 10\,\text{cm}$, $N^{\text{r}} = 200$, and $N^{\text{p}} = 25$.

Fig. 3 (a) compares the surface profiles reconstructed at 350 MHz, 800 MHz, and 900 MHz to $s^{\text{ref}}(x)$. The figure shows that reconstructions at 800 MHz and 900 MHz cannot be easily distinguished by naked eye and are closer to $s^{\text{ref}}(x)$ than the construction at 350 MHz. Fig. 3 (b) plots $err_{(m)}$ versus frequency. It is apparent that the error drops and the quality of the reconstruction increases with increasing frequency.

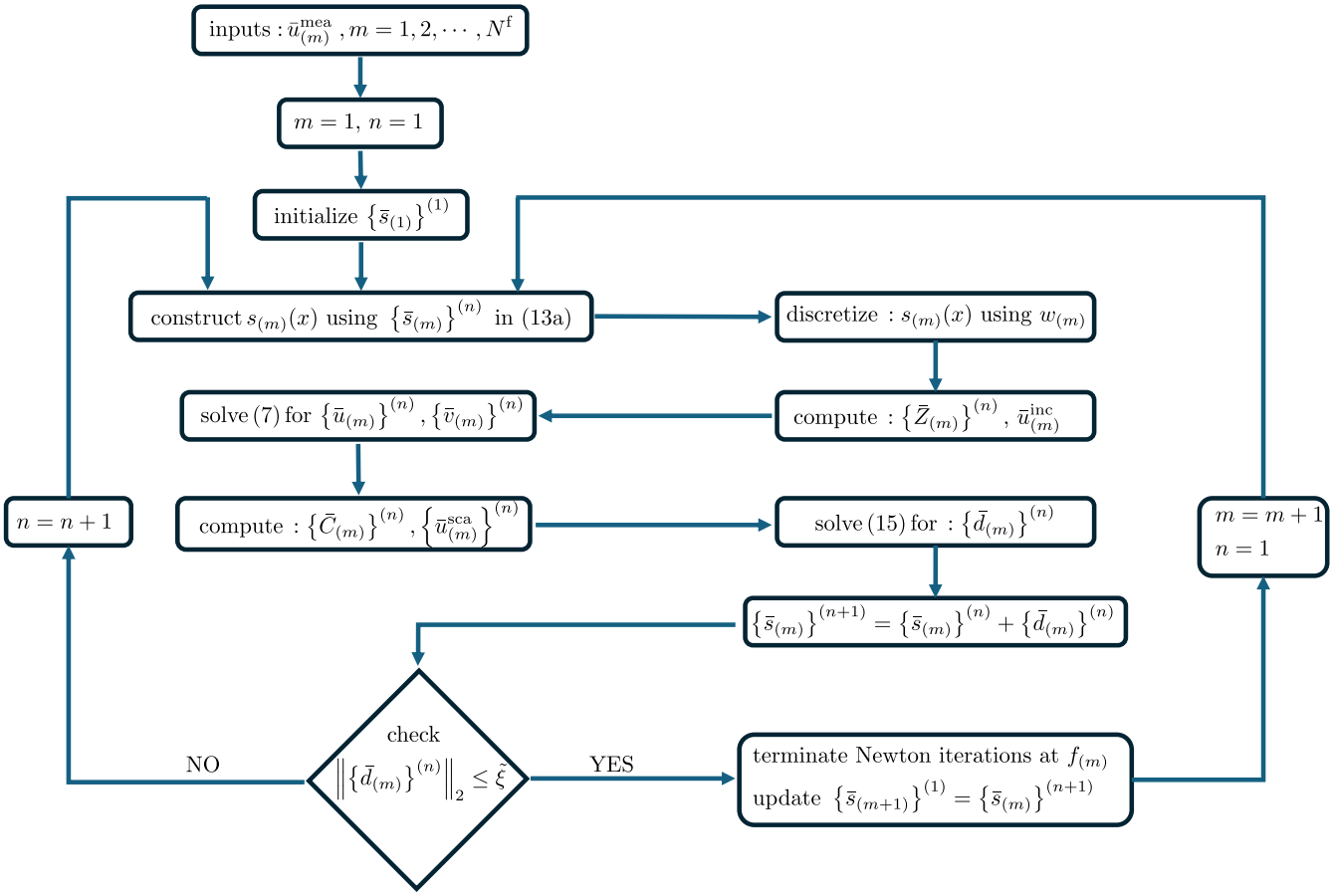

FIGURE 2. Flowchart describing the algorithm for the multi-frequency Newton iterations.

B. SINGLE VERSUS MULTI-FREQUENCY RECONSTRUCTION

This example demonstrates that the inclusion of multi-frequency data in the reconstruction increases its accuracy. $s^{\text{ref}}(x)$ is generated with $\ell = 0.55$ m and $h = 0.06$ m. Two simulations are carried out. In the first simulation (multi-frequency), the simulation parameters are $A_{\text{n}} = 0$ (no noise), $f_{\text{sta}} = 400$ MHz, $f_{\text{end}} = 600$ MHz, $\Delta f = 25$ MHz, $\Delta x^{\text{r}} = 20$, $N^{\text{r}} = 100$, and $N^{\text{p}} = 20$. The parameters of the second simulation are same as the first one except the frequency. For the second simulation, the reconstruction is carried out only at a single frequency 600 MHz.

Fig. 4 compares the surface profiles reconstructed by the first (multi-frequency) and the second (single-frequency) simulations at 600 MHz to $s^{\text{ref}}(x)$. As shown in the figure, multi-frequency simulation produces a much more accurate reconstruction. This example clearly demonstrates the benefits of including multi-frequency data in the iterative reconstruction process.

C. DEPENDENCE ON FREQUENCY SAMPLING

In this example, the dependence of the reconstruction accuracy on the frequency sampling is investigated. $s^{\text{ref}}(x)$ is generated with $\ell = 0.4$ m and $h = 0.07$ m. Five simulations are carried out. The following parameters are kept the same in all five simulations: $A_{\text{n}} = 0$ (no noise), $f_{\text{sta}} = 300$ MHz, $f_{\text{end}} = 600$ MHz, $\Delta x^{\text{r}} = 10$ cm, $N^{\text{r}} = 200$, and $N^{\text{p}} = 17$. Then in each simulation Δf is set to a different value: $\Delta f \in \{10, 20, 50, 150, 300\}$ MHz (corresponding to $N^{\text{f}} \in \{31, 16, 7, 3, 2\}$ number of frequency samples, respectively).

Fig. 5 (a) plots $err_{(m)}$ versus frequency for all five simulations. The figure shows that smaller Δf yields a more accurate reconstruction at f_{end} (set to 600 MHz in this case). But this increase in accuracy saturates: The reconstructions at 600 MHz obtained by simulations with $\Delta f = 10$ MHz to $\Delta f = 50$ MHz reach roughly the same error level. This is also demonstrated by Fig. 5 (b) where the surface profiles reconstructed by the simulations with $\Delta f = 10$ MHz, $\Delta f = 20$ MHz, and $\Delta f = 300$ MHz at 600 MHz are compared to $s^{\text{ref}}(x)$. The reconstructions with $\Delta f = 10$ MHz and $\Delta f = 50$ MHz are very close to $s^{\text{ref}}(x)$ while the reconstruction with $\Delta f = 300$ MHz is not.

D. SURFACE PROFILE WITH SHARP VARIATIONS

For this example, the performance of the multi-frequency Newton iterations in reconstructing a surface profile with

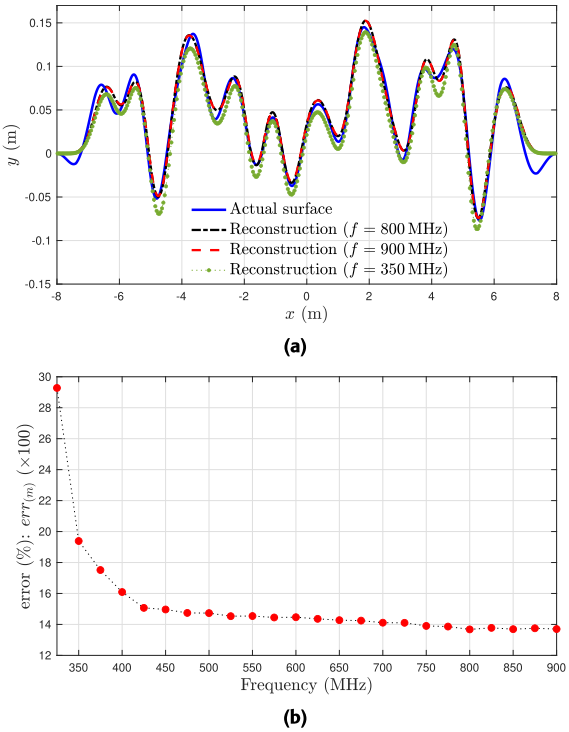

FIGURE 3. Example in Section III-A. (a) Actual surface profile and the reconstructions at 350 MHz, 800 MHz, and 900 MHz. (b) Error in reconstruction computed using (22) versus frequency.

sharp variations. To this end, $s^{\text{ref}}(x)$ is generated using triangular functions

$$s^{\text{ref}}(x) = \begin{cases} x+4, & \text{if } -6 \le x \le -3 \\ x, & \text{if } 0 \le x \le 2 \\ 4-x, & \text{if } 2 \le x < 4 \\ 0, & \text{otherwise} \end{cases} \tag{23}$$

Two simulations are carried out. In the first simulation (multi-frequency), the parameters are $A_{\text{n}} = 0$ (no noise), $f_{\text{sta}} = 400\,\text{MHz}$, $f_{\text{end}} = 800\,\text{MHz}$, $\Delta f = 20\,\text{MHz}$, $\Delta x^{\text{r}} = 10\,\text{cm}$, $N^{\text{r}} = 200$, and $N^{\text{p}} = 18$. The parameters of the second simulation are same as the first one except the frequency. For the second simulation, the reconstruction is carried out only at a single frequency 800 MHz.

Fig. 6 compares the surface profiles reconstructed by the first (multi-frequency) and the second (single-frequency) simulations at 800 MHz to $s^{\text{ref}}(x)$. As expected, multi-frequency reconstruction is significantly more accurate. Single-frequency reconstruction can not capture the sharp variations at all.

E. DEPENDENCE ON NOISE

In this example, the performance of the multi-frequency Newton iterations is investigated for measurement data that is contaminated by different levels of noise. $s^{\text{ref}}(x)$ is generated with $\ell = 0.5\,\text{m}$ and $h = 0.05\,\text{m}$. Eleven simulations are carried out. The following parameters are kept the same in all eleven simulations: $f_{\text{sta}} = 425\,\text{MHz}$, $f_{\text{end}} = 675\,\text{MHz}$, $\Delta f = 25\,\text{MHz}$, $\Delta x^{\text{r}} = 10\,\text{cm}$, $N^{\text{r}} = 200$, and $N^{\text{p}} = 18$. Then in each simulation A_{n} is set to a different value: $A_{\text{n}} \in \{3, 5, 7, 10, 12, 15, 20, 25, 30, 35, 40, 45, 50\}\%$.

Fig. 7 (a) plots $err_{(11)}$ computed at $f_{\text{end}} = 675\,\text{MHz}$ by each of these simulations versus the noise level. Fig. 7 (b) compares the surface profiles reconstructed by the simulations with $A_{\text{n}} = 3\%$, $A_{\text{n}} = 35\%$, and $A_{\text{n}} = 50\%$ to $s^{\text{ref}}(x)$. As expected, the measurements that are contaminated the least lead to the most accurate constructions. It can be deducted from Figs. 7 (a) and (b) that the multi-frequency

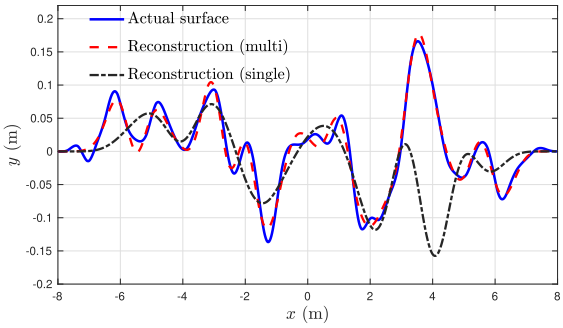

FIGURE 4. Example in Section III-B. Actual surface profile and the reconstructions obtained by the multi- and single-frequency simulations at 600 MHz.

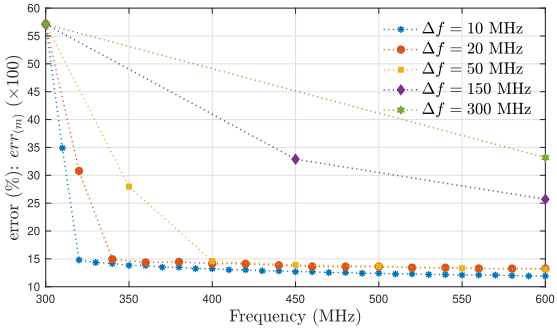

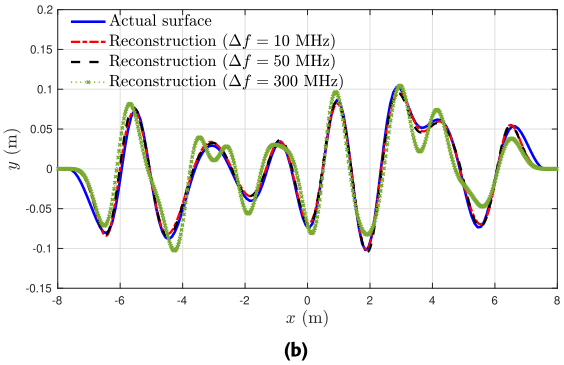

FIGURE 5. Example in Section III-C. (a) Error in reconstruction computed using (22) versus frequency for the simulations with the frequency increment 10 MHz, 20 MHz, 50 MHz, 150 MHz, 300 MHz. (b) Actual surface profile and the reconstructions obtained by the simulations with the frequency increment 10 MHz, 50 MHz, and 300 MHz at 600 MHz.

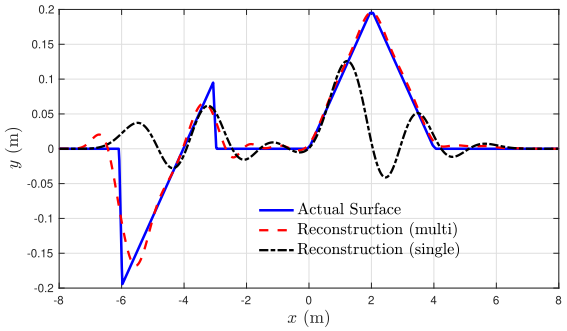

FIGURE 6. Example in Section III-D. Actual surface profile and the reconstructions obtained by the multi- and single-frequency simulations at 800 MHz.

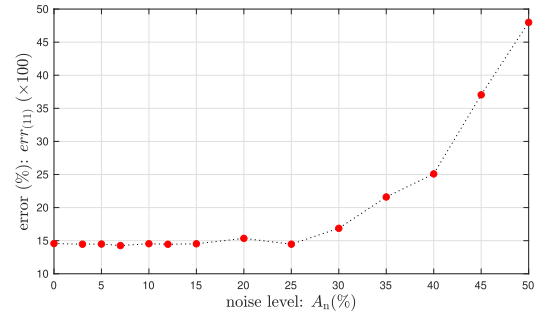

(a)

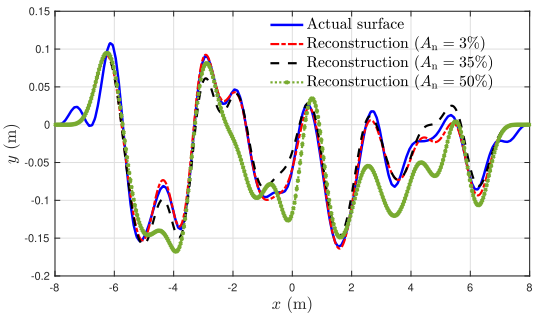

(b)

FIGURE 7. Example in Section III-E. (a) Error in reconstruction at 675 MHz computed using (22) versus noise level. (b) Actual surface profile and the reconstructions obtained by the simulations with noise level 3%, 35%, and 50% at 675 MHz.

Newton iterations are rather robust to the noise in the measurements.

F. COMPUTATION TIME

In this section, computation time requirement of the multi-frequency Newton iterations is investigated using two examples. In the first example, $s^{\text{ref}}(x)$ is generated with $\ell = 0.35\,\text{m}$ and $h = 0.75\,\text{m}$. The simulation parameters are $A_n = 0$ (no noise), $f_{\text{sta}} = 400\,\text{MHz}$, $f_{\text{end}} = 650\,\text{MHz}$, $\Delta f = 25\,\text{MHz}$, $N^r = 200$ with $\Delta x^r = 10\,\text{cm}$ and $N^p = 29$. Fig. 8 (a) plots the CPU time required by the Newton iterations to converge versus frequency. The figure shows that the CPU time per frequency decreases after 500 MHz even though the computational cost of solving (7)

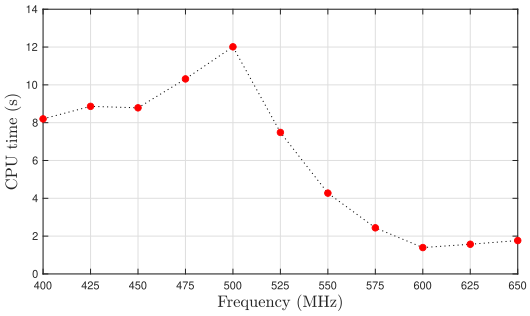

(a)

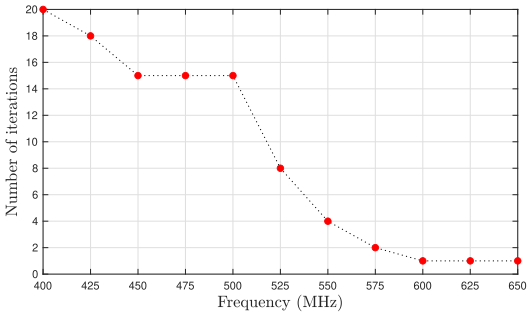

(b)

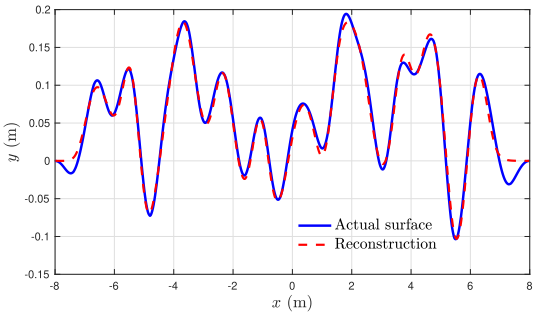

(c)

FIGURE 8. First example in Section III-F (a) Time required by the Newton iterations to converge versus frequency. (b) Number of iterations required for convergence versus frequency. (c) Actual surface profile and the reconstruction at 650 MHz.

increases with frequency (because $w_{(m)}$ decreases and $N^s_{(m)}$ increases). This decrease in the CPU time is explained by the fact that the number of Newton iterations decreases because the reconstruction at one frequency is used as the initial guess for the next one. This is shown in Fig. 8 (b), which plots the number of iterations required for convergence versus frequency. Fig. 8 (c) demonstrates the accuracy of the reconstruction at the last frequency sample of 650 MHz by comparing it to s^{ref}. For the first example, single-frequency Newton iterations do not converge except only at the first frequency, but the resolution of the reconstruction at this frequency is not high enough to accurately capture the variations in the actual surface.

In the second example, a ''simpler'' surface with smaller variations is selected to ensure that the single-frequency Newton iterations can obtain an accurate reconstruction.

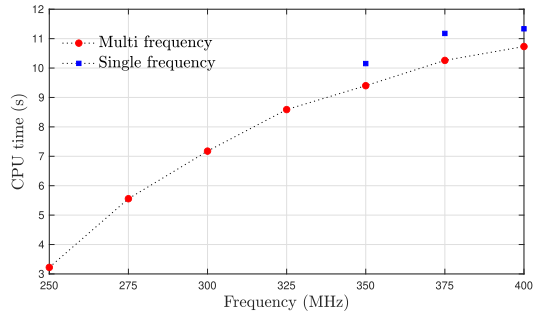

(a)

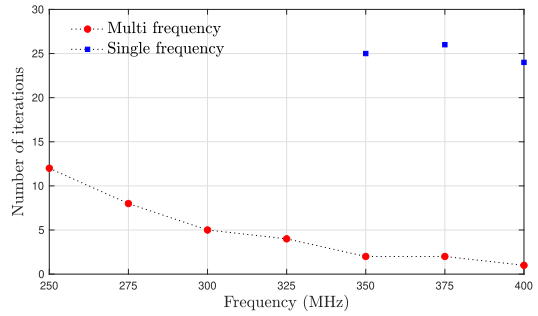

(b)

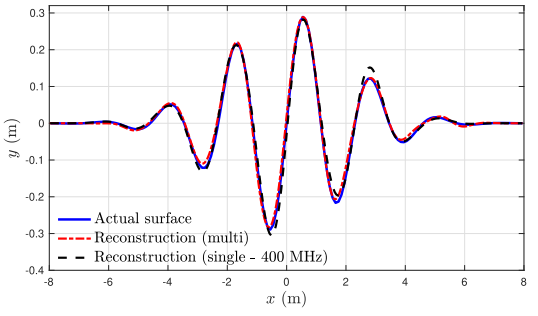

(c)

FIGURE 9. Second example in Section III-F. (a) Cumulative CPU time required by the multi-frequency Newton iterations to obtain the reconstruction a given frequency (which includes the time required at previous frequencies) and the CPU time required by the individual executions of the single-frequency Newton iterations. (b) Number of iterations required by the multi- and single-frequency Newton iterations for convergence versus frequency. (c) Actual surface profile and the reconstructions obtained by the multi- and single-frequency Newton iterations at 400 MHz.

To this end, $s^{\text{ref}}(x)$ is generated using

$$s^{\text{ref}}(x) = 0.1\,[\sin(0.8\pi x) + 2\sin(0.9\pi x)]\,e^{0.1x^2}. \qquad (24)$$

The simulation parameters for both multi- and single-frequency methods are $A_{\text{n}} = 0$ (no noise), $\Delta x^{\text{r}} = 10\,\text{cm}$, and $N^{\text{r}} = 200$, and $N^{\text{p}} = 14$. For the multi-frequency method the frequency range is from $f_{\text{sta}} = 250\,\text{MHz}$ to $f_{\text{end}} = 400\,\text{MHz}$ with a step of $\Delta f = 25\,\text{MHz}$. The single-frequency method is executed at the last three samples within this range: 350 MHz, 375 MHz, and 400 MHz. Fig. 9 (a) plots the cumulative CPU time required by the multi-frequency Newton iterations to obtain the reconstruction a given frequency (which includes the time required at previous

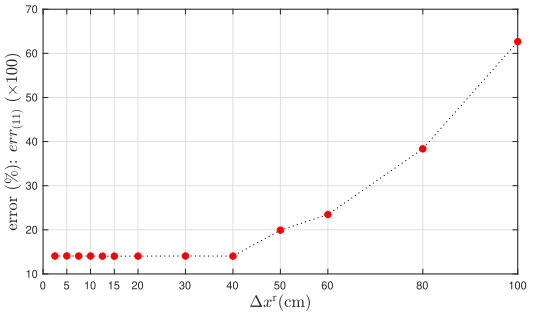

(a)

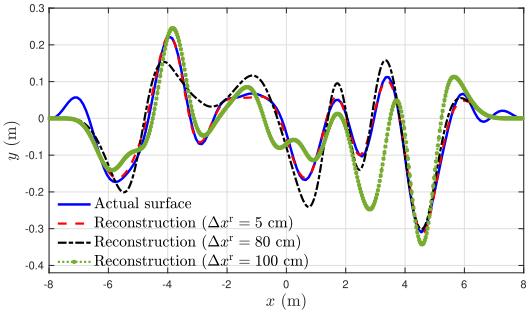

(b)

FIGURE 10. Example in Section III-G. (a) Error in reconstruction at 500 MHz computed using (22) versus the measurement point spacing. (b) Actual surface profile and the reconstructions obtained by the simulations with the measurement point spacing 5 cm, 80 cm, and 100 cm at 500 MHz.

frequencies) to the CPU time required by the individual executions of the single-frequency Newton iterations. The figure shows that the multi-frequency Newton iterations are faster than the single-frequency Newton iterations. This is expected because the number of iterations required by the multi-frequency method are smaller than those required by the single-frequency method due to the use of reconstruction at the previous frequency as initial guess (see Fig. 9 (b) for the comparison of number of iterations). Fig. 9 (c) compares the reconstructions obtained by the single- and multi-frequency Newton iterations at 400 MHZ to s^{ref}. The errors in these two reconstructions as computed using (22) are 13.37% and 6.31% for the single- and the multi-frequency cases, respectively. Fig. 9 clearly demonstrates that multi-frequency Newton iterations achieve a more accurate reconstruction in a shorter time.

G. DEPENDENCE ON THE NUMBER OF MEASUREMENTS

In the last example, the performance of the multi-frequency Newton iterations is investigated for different numbers of measurement points. $s^{\text{ref}}(x)$ is generated with $\ell = 0.7\,\text{m}$ and $h = 0.08\,\text{m}$. Twelve simulations are carried out. The following parameters are kept the same in all twelve simulations: $A_{\text{n}} = 0$ (no noise), $f_{\text{sta}} = 300\,\text{MHz}$, $f_{\text{end}} = 500\,\text{MHz}$, $\Delta f = 20\,\text{MHz}$, and $N^{\text{p}} = 18$. Then in each simulation Δx^{r} is set to a different value: $\Delta x^{\text{r}} \in \{2.5, 5, 7.5, 10, 15, 20, 30, 40, 50, 60, 80, 100\}$ cm (corresponding to $N^{\text{r}} \in \{800, 400, 266, 200, 133, 100, 66, 50, 40, 33, 25, 20\}$ number of measurement points, respectively).

Fig. 10 (a) plots $err_{(11)}$ versus frequency for all twelve simulations. Fig. 10 (b) compares the surface profiles reconstructed by the simulations with $\Delta x^{\mathrm{r}} = 5\,\mathrm{cm}$, $\Delta x^{\mathrm{r}} = 80\,\mathrm{cm}$, and $\Delta x^{\mathrm{r}} = 100\,\mathrm{cm}$ at 500 MHz to $s^{\mathrm{ref}}(x)$.

IV. CONCLUSION

A numerical scheme that utilizes multi-frequency Newton iterations to reconstruct rough surface profiles between two dielectric media is presented. At each frequency sample, the scheme applies Newton iterations to solve the nonlinear inverse scattering problem. In each iteration, the Newton step is determined by solving a linear system that involves the Frechet derivative of the integral operator, which models the scattered fields, and the difference between these fields and the measured data. This linear system is regularized using the Tikhonov method.

The scheme accounts for multi-frequency data in a recursive manner, using the profile reconstructed at one frequency as the initial guess for the next frequency's iterations. Numerical examples validate the effectiveness of the proposed method, demonstrating its capability to accurately reconstruct surface profiles even in the presence of measurement noise. The results also highlight the superiority of the multi-frequency approach over single-frequency reconstructions, particularly in handling surfaces with sharp variations.

The proposed algorithm can be extended to address layered media problems, where multiple rough surfaces separate more than two media, as well as to 3D surface imaging problems. These extensions are considered for future work.

APPENDIX A

The pulse basis functions $f_i(x)$, $i = 1, 2, \ldots, N^{\mathrm{s}}$ in expansions (6a) and (6b) are defined as

$$f_i(x) = \begin{cases} 1 & \text{for } (x_i^{\mathrm{s}} - w/2) \le x \le (x_i^{\mathrm{s}} + w/2) \\ 0 & \text{otherwise.} \end{cases} \tag{25}$$

The elements of the vector of tested incident field $\bar{u}^{\mathrm{inc}}$ in (7) are

$$\bar{u}_j^{\mathrm{inc}} = u^{\mathrm{inc}}(x_j^{\mathrm{s}}, s(x_j^{\mathrm{s}})), \quad j = 1, 2, \ldots, N^{\mathrm{s}}. \tag{26}$$

The midpoint integration is used to evaluate the surface integrals over segment i, which arise from the discretization of (5a) and (5b). This leads to the following expressions for the elements of the impedance matrix $\bar{Z}$ in (7) [15]

$$\bar{Z}_{ji}^{11} = \begin{cases} -w_i K_1(\mathbf{r}_j^{\mathrm{s}}, \mathbf{r}_i^{\mathrm{s}}) & \text{for } j \ne i \\ \dfrac{1}{2} & \text{for } j = i \end{cases} \tag{27a}$$

$$\bar{Z}_{ji}^{12} = w_i \begin{cases} G_1(\mathbf{r}_j^{\mathrm{s}}, \mathbf{r}_i^{\mathrm{s}}) & \text{for } j \ne i \\ \dfrac{\mathrm{i}}{4} - \dfrac{1}{2\pi}\left[(\gamma - 1) + \ln\left(\dfrac{k_1 w_i}{4}\right)\right] & \text{for } j = i \end{cases} \tag{27b}$$

$$\bar{Z}_{ji}^{21} = \begin{cases} w_i K_2(\mathbf{r}_j^{\mathrm{s}}, \mathbf{r}_i^{\mathrm{s}}) & \text{for } j \ne i \\ \dfrac{1}{2} & \text{for } j = i \end{cases} \tag{27c}$$

$$\bar{Z}_{ji}^{22} = -w_i \begin{cases} G_2(\mathbf{r}_j^{\mathrm{s}}, \mathbf{r}_i^{\mathrm{s}}) & \text{for } j \ne i \\ \dfrac{\mathrm{i}}{4} - \dfrac{1}{2\pi}\left[(\gamma - 1) + \ln\left(\dfrac{k_2 w_i}{4}\right)\right] & \text{for } j = i \end{cases} \tag{27d}$$

$i, j = 1, 2, \ldots, N^{\mathrm{s}}$. Here, $w_i = w\sqrt{1 + s(x_i^{\mathrm{s}})^2}$ is the length of the surface corresponding to segment i and γ is the Euler's constant. To obtain the expressions for $j = i$ in (27b) and (27d), the small argument approximation of the Hankel function $H_0^{(1)}(.)$ is used [48].

APPENDIX B

The spline-type basis functions $\phi(x)_i$, $i = 1, 2, \ldots, N^{\mathrm{p}}$ used in expansions (13a) and (13b) are defined as [30], [49], [50], [51], and [52]

$$\phi_i(x) = \phi([x - x_i]/g), \tag{28}$$

where $g = L/2(N^{\mathrm{p}} + 5)$, $x_i = (i + 2)(g - L/2)$, and

$$\phi(x) = \begin{cases} \displaystyle\sum_{q=0}^{p+1} \frac{(-1)^q}{p!} \binom{p+1}{q} \left(x + \frac{p+1}{2} - q\right)^p \\ \qquad \text{for } \left(x + \dfrac{p+1}{2}\right) \ge q \\ 0, \qquad \text{otherwise.} \end{cases} \tag{29}$$

Here, p is the order of the spline functions.

The elements of the matrix $\bar{C}$ in (14) are

$$\begin{aligned} C_{ji} = &- \int_{\Gamma(s)} \partial_s G_1(\mathbf{r}, \mathbf{r}')\Big|_{\mathbf{r}=(x_j^{\mathrm{r}}, \alpha)} v(\mathbf{r}')\phi_i(\mathbf{r}')dl' \\ &+ \int_{\Gamma(s)} \partial_s K_1(\mathbf{r}, \mathbf{r}')\Big|_{\mathbf{r}=(x_j^{\mathrm{r}}, \alpha)} u(\mathbf{r}')\phi_i(\mathbf{r}')dl' \\ &j = 1, 2, \ldots, N^{\mathrm{r}}, \ i = 1, 2, \ldots, N^{\mathrm{p}}. \end{aligned} \tag{30}$$

Here, "∂_s" represents the derivative with respective to s, and explicit expressions of $\partial_s G_1(\mathbf{r}, \mathbf{r}')$ and $\partial_s K_1(\mathbf{r}, \mathbf{r}')$ are given in [29]. The integral in (30) is evaluated using the trapezoidal integration rule.

The midpoint integration is used to evaluate the surface integrals over segment i which arise from the discretization of $\mathcal{D}[s, u, v](x_j^{\mathrm{r}}, \alpha)$ in (12). This leads to following expression for the elements of the vector $\bar{u}^{\mathrm{sca}}$ in (14)

$$\begin{aligned} \bar{u}_j^{\mathrm{sca}} = &\sum_{i=1}^{N^{\mathrm{s}}} \bar{u}_i w_i K_1(\mathbf{r}_j^{\mathrm{r}}, \mathbf{r}_i^{\mathrm{s}}) - \sum_{i=1}^{N^{\mathrm{s}}} \bar{v}_i w_i G_1(\mathbf{r}_j^{\mathrm{r}}, \mathbf{r}_i^{\mathrm{s}}) \\ &j = 1, 2, \ldots, N^{\mathrm{r}}. \end{aligned} \tag{31}$$

REFERENCES

[1] P. Marzahn, D. Rieke-Zapp, and R. Ludwig, "Assessment of soil surface roughness statistics for microwave remote sensing applications using a simple photogrammetric acquisition system," *ISPRS J. Photogramm. Remote Sens.*, vol. 72, pp. 80–89, Aug. 2012.

[2] P. Marzahn and R. Ludwig, "On the derivation of soil surface roughness from multi parametric PolSAR data and its potential for hydrological modeling," *Hydrol. Earth Syst. Sci.*, vol. 13, no. 3, pp. 381–394, Mar. 2009.
[3] I. Hajnsek, T. Jagdhuber, H. Schon, and K. P. Papathanassiou, "Potential of estimating soil moisture under vegetation cover by means of PolSAR," *IEEE Trans. Geosci. Remote Sens.*, vol. 47, no. 2, pp. 442–454, Feb. 2009.
[4] S. Labarre, S. Jacquemoud, C. Ferrari, A. Delorme, A. Derrien, R. Grandin, M. Jalludin, F. Lemaêtre, M. Métois, M. Pierrot-Deseilligny, E. Rupnik, and B. Tanguy, "Retrieving soil surface roughness with the Hapke photometric model: Confrontation with the ground truth," *Remote Sens. Environ.*, vol. 225, pp. 1–15, May 2019.
[5] L. Zhao, L. Wu, and Y. Fang, "Surface reconstruction and thickness error calculation of optical components with a complex curved surface," *Appl. Opt.*, vol. 63, no. 11, pp. 2922–2929, Apr. 2024.
[6] H. Ye and Y.-Q. Jin, "An inversion of planetary rough surface permittivity from radar sounder observations," *IEEE Antennas Wireless Propag. Lett.*, vol. 12, pp. 1069–1072, 2013.
[7] Ö. Özdemir and Y. Altuncu, "A microwave subsurface imaging technique for rough surfaces," *IEEE Geosci. Remote Sens. Lett.*, vol. 20, pp. 1–5, 2023.
[8] M. Salucci, C. Estatico, A. Fedeli, G. Oliveri, M. Pastorino, S. Povoli, A. Randazzo, and P. Rocca, "2-D TM GPR imaging through a multiscaling multifrequency approach in L_p spaces," *IEEE Trans. Geosci. Remote Sens.*, vol. 59, no. 12, pp. 10011–10021, Dec. 2021.
[9] A. J. C. Jarvis and F. B. Cegla, "Application of the distributed point source method to rough surface scattering and ultrasonic wall thickness measurement," *J. Acoust. Soc. Amer.*, vol. 132, no. 3, pp. 1325–1335, Sep. 2012.
[10] Z. Wang, F. Shi, and F. Zou, "Deep learning based ultrasonic reconstruction of rough surface morphology," *Ultrasonics*, vol. 138, Mar. 2024, Art. no. 107265.
[11] J. Zhang, J. Wu, X. Zhao, S. Yuan, G. Ma, J. Li, T. Dai, H. Chen, B. Yang, and H. Ding, "Laser ultrasonic imaging for defect detection on metal additive manufacturing components with rough surfaces," *Appl. Opt.*, vol. 59, no. 33, p. 10380, Nov. 2020.
[12] J. R. Pettit, A. E. Walker, and M. J. S. Lowe, "Improved detection of rough defects for ultrasonic nondestructive evaluation inspections based on finite element modeling of elastic wave scattering," *IEEE Trans. Ultrason., Ferroelectr., Freq. Control*, vol. 62, no. 10, pp. 1797–1808, Oct. 2015.
[13] W. Choi, F. Shi, M. J. S. Lowe, E. A. Skelton, R. V. Craster, and W. L. Daniels, "Rough surface reconstruction of real surfaces for numerical simulations of ultrasonic wave scattering," *NDT & E Int.*, vol. 98, pp. 27–36, Sep. 2018.
[14] F. Shi, M. J. S. Lowe, and R. V. Craster, "Recovery of correlation function of internal random rough surfaces from diffusely scattered elastic waves," *J. Mech. Phys. Solids*, vol. 99, pp. 483–494, Feb. 2017.
[15] L. Tsang, J. A. Kong, K.-H. Ding, and C. O. Ao, *Scattering of Electromagnetic Waves: Numerical Simulations*, 1st ed., Hoboken, NJ, USA: Wiley, 2001.
[16] D. Colton and R. Kress, *Inverse Acoustic and Electromagnetic Scattering Theory*, 2nd ed., Berlin, Germany: Springer-Verlag, 1998.
[17] D. Colton and R. Kress, "Looking back on inverse scattering theory," *SIAM Rev.*, vol. 60, no. 4, pp. 779–807, Jan. 2018.
[18] G. Dolcetti, M. Alkmim, J. Cuenca, L. De Ryck, and A. Krynkin, "Robust reconstruction of scattering surfaces using a linear microphone array," *J. Sound Vib.*, vol. 494, Mar. 2021, Art. no. 115902.
[19] R. J. Wombell and J. A. DeSanto, "The reconstruction of shallow rough-surface profiles from scattered field data," *Inverse Problems*, vol. 7, no. 1, pp. L7–L12, Feb. 1991.
[20] A. Schatzberg and A. J. Devaney, "Rough surface inverse scattering within the Rytov approximation," *J. Opt. Soc. Amer. A, Opt. Image Sci.*, vol. 10, no. 5, p. 942, May 1993.
[21] G. Bao and P. Li, "Near-field imaging of infinite rough surfaces in dielectric media," *SIAM J. Imag. Sci.*, vol. 7, no. 2, pp. 867–899, Jan. 2014.
[22] A. Sefer, A. Yapar, and T. Yelkenci, "Imaging of rough surfaces by RTM method," *IEEE Trans. Geosci. Remote Sens.*, vol. 62, 2024, Art. no. 2003312.
[23] Y. Chen and M. Spivack, "Rough surface reconstruction at grazing angles by an iterated marching method," *J. Opt. Soc. Amer. A, Opt. Image Sci.*, vol. 35, no. 4, pp. 504–513, 2018.
[24] Y. Chen, O. Rath Spivack, and M. Spivack, "Rough surface reconstruction from phaseless single frequency data at grazing angles," *Inverse Problems*, vol. 34, no. 12, Dec. 2018, Art. no. 124002.
[25] Y. Chen, M. Spivack, and O. Rath Spivack, "Reconstruction of rough surfaces from a single receiver at grazing angle," *IET Sci., Meas. Technol.*, vol. 18, no. 7, pp. 361–372, Sep. 2024.
[26] G. Bao, P. Li, and J. Lv, "Numerical solution of an inverse diffraction grating problem from phaseless data," *J. Opt. Soc. Amer. A, Opt. Image Sci.*, vol. 30, no. 3, pp. 293–299, 2013.
[27] G. Bao and L. Zhang, "Shape reconstruction of the multi-scale rough surface from multi-frequency phaseless data," *Inverse Problems*, vol. 32, no. 8, Aug. 2016, Art. no. 085002.
[28] L. Chorfi and P. Gaitan, "Reconstruction of the interface between two-layered media using far field measurements," *Inverse Problems*, vol. 27, no. 7, Jul. 2011, Art. no. 075001.
[29] A. Sefer and A. Yapar, "An iterative algorithm for imaging of rough surfaces separating two dielectric media," *IEEE Trans. Geosci. Remote Sens.*, vol. 59, no. 2, pp. 1041–1051, Feb. 2021.
[30] J. Li and G. Sun, "A nonlinear integral equation method for the inverse scattering problem by sound-soft rough surfaces," *Inverse Problems Sci. Eng.*, vol. 23, no. 4, pp. 557–577, May 2015.
[31] A. Sefer, "Locally perturbed inaccessible rough surface profile reconstruction via phaseless scattered field data," *IEEE Trans. Geosci. Remote Sens.*, vol. 60, 2022, Art. no. 2002808.
[32] A. Sefer and A. Yapar, "Image recovery of inaccessible rough surfaces profiles having impedance boundary condition," *IEEE Geosci. Remote Sens. Lett.*, vol. 19, pp. 1–5, 2022.
[33] O. M. Bucci, L. Crocco, T. Isernia, and V. Pascazio, "Inverse scattering problems with multifrequency data: Reconstruction capabilities and solution strategies," *IEEE Trans. Geosci. Remote Sens.*, vol. 38, no. 4, pp. 1749–1756, Jul. 2000.
[34] W. C. Chew and J. H. Lin, "A frequency-hopping approach for microwave imaging of large inhomogeneous bodies," *IEEE Microw. Guided Wave Lett.*, vol. 5, no. 12, pp. 439–441, Dec. 1995.
[35] M. Salucci, G. Oliveri, and A. Massa, "GPR prospecting through an inverse-scattering frequency-hopping multifocusing approach," *IEEE Trans. Geosci. Remote Sens.*, vol. 53, no. 12, pp. 6573–6592, Dec. 2015.
[36] M. Salucci and N. Anselmi, "Multi-frequency GPR microwave imaging of sparse targets through a multi-task Bayesian compressive sensing approach," *J. Imag.*, vol. 7, no. 11, p. 247, Nov. 2021.
[37] Y. Zhong, M. Salucci, K. Xu, A. Polo, and A. Massa, "A multiresolution contraction integral equation method for solving highly nonlinear inverse scattering problems," *IEEE Trans. Microw. Theory Techn.*, vol. 68, no. 4, pp. 1234–1247, Apr. 2020.
[38] S. Takahashi, K. Suzuki, T. Hanabusa, and S. Kidera, "Microwave subsurface imaging method by incorporating radar and tomographic approaches," *IEEE Trans. Antennas Propag.*, vol. 70, no. 11, pp. 11009–11023, Nov. 2022.
[39] M. Hajebi and A. Hoorfar, "Multiple buried target reconstruction using a multiscale hybrid of diffraction tomography and CMA-ES optimization," *IEEE Trans. Geosci. Remote Sens.*, vol. 60, 2022, Art. no. 2006713.
[40] E. I. Thorsos, "The validity of the Kirchhoff approximation for rough surface scattering using a Gaussian roughness spectrum," *J. Acoust. Soc. Amer.*, vol. 83, no. 1, pp. 78–92, Jan. 1988.
[41] M. Born and E. Wolf, *Principles of Optics: Electromagnetic Theory of Propagation, Interference and Diffraction of Light*, 7th ed., Cambridge, U.K.: Cambridge Univ. Press, 1999.
[42] D. Zwillinger, *CRC Standard Mathematical Tables and Formulae* (Advances in applied mathematics), 30th ed., Orlando, FL, USA: CRC Press, 1996.
[43] H.-T. Chou and J. T. Johnson, "A novel acceleration algorithm for the computation of scattering from rough surfaces with the forward-backward method," *Radio Sci.*, vol. 33, no. 5, pp. 1277–1287, Sep. 1998.
[44] N. Dechamps and C. Bourlier, "Electromagnetic scattering from a rough layer: Propagation-inside-layer expansion method combined to the forward-backward novel spectral acceleration," *IEEE Trans. Antennas Propag.*, vol. 55, no. 12, pp. 3576–3586, Dec. 2007.
[45] L. Tsang, C. H. Chan, K. Pak, and H. Sangani, "Monte–Carlo simulations of large-scale problems of random rough surface scattering and applications to grazing incidence with the BMIA/canonical grid method," *IEEE Trans. Antennas Propag.*, vol. 43, no. 8, pp. 851–859, Aug. 1995.
[46] V. Jandhyala, B. Shanker, E. Michielssen, and W. C. Chew, "Fast algorithm for the analysis of scattering by dielectric rough surfaces," *J. Opt. Soc. Amer. A, Opt. Image Sci.*, vol. 15, no. 7, pp. 1877–1885, Jul. 1998.

[47] Q. Li and L. Tsang, "Wave scattering from lossy dielectric random rough surfaces using the physics-based two-grid method in conjunction with the multilevel fast multipole method," *Radio Sci.*, vol. 36, no. 4, pp. 571–583, Jul. 2001.
[48] M. Abramowitz and I. A. Stegun, *Handbook of Mathematical Functions, With Formulas, Graphs, and Mathematical Tables*, 31th ed., New York, NY, USA: Dover, 1974, pp. 355–360.
[49] C. D. Boor, *A Practical Guide To Splines*. New York, NY USA: Springer-Verlag, 1978.
[50] J. Li, G. Sun, and B. Zhang, "The Kirsch–Kress method for inverse scattering by infinite locally rough interfaces," *Applicable Anal.*, vol. 96, no. 1, pp. 85–107, Jan. 2017.
[51] H. Zhang and B. Zhang, "A novel integral equation for scattering by locally rough surfaces and application to the inverse problem," *SIAM J. Appl. Math.*, vol. 73, no. 5, pp. 1811–1829, Jan. 2013, doi: 10.1137/130908324.
[52] İ. Aydin, G. Budak, A. Sefer, and A. Yapar, "Recovery of impenetrable rough surface profiles via CNN-based deep learning architecture," *Int. J. Remote Sens.*, vol. 43, nos. 15–16, pp. 5658–5685, Aug. 2022.

AHMET SEFER (Member, IEEE) received the B.Sc. degree in electrical and electronics engineering from Bilkent University, Ankara, Türkiye, in 2010, and the Ph.D. degree from the Graduate School, Istanbul Technical University, Istanbul, Türkiye, in 2021. Since September 2021, he has been an Assistant Professor with the Department of Electrical and Electronics Engineering, FMV Isik University, Istanbul. Since March 2023, he has been a Postdoctoral Fellow with the King Abdullah University of Science and Technology (KAUST), Saudi Arabia. His current research interests include electromagnetic theory, direct and inverse scattering problems, microwave imaging, integral equations, and numerical techniques in electromagnetics. He was a recipient of Leopold B. Felsen Excellence in Electrodynamics Award from Leopold B. Felsen Fund, in 2020. He is currently a member of the IEEE Antennas and Propagation Society and IEEE Geoscience and Remote Sensing Society. He has been the Chair of IEEE Antennas and Propagation Society-Istanbul Chapter.

ALI YAPAR was born in Akşehir, Türkiye, in 1973. He received the B.Sc. degree in electrical engineering and in mathematics and the M.Sc. and Ph.D. degrees in electronics and communication engineering from Istanbul Technical University, Istanbul, Türkiye, in 1995, 1997, and 2001, respectively. From 2001 to 2002, he was a Visiting Scientist with the University of Illinois at Urbana–Champaign, Champaign, IL, USA. He is currently a Professor with Istanbul Technical University. His research interests include electromagnetic theory, direct and inverse scattering problems, microwave imaging, integral equations, and numerical techniques.

HAKAN BAGCI (Senior Member, IEEE) received the B.S. degree in electrical and electronics engineering from Bilkent University, Ankara, Türkiye, in 2001, and the M.S. and Ph.D. degrees in electrical and computer engineering from the University of Illinois at Urbana–Champaign (UIUC), Urbana, IL, USA, in 2003 and 2007, respectively.

From June 1999 to July 2001, he was an Undergraduate Researcher with the Computational Electromagnetics Group, Bilkent University. From August 2001 to December 2006, he was a Research Assistant with the Center for Computational Electromagnetics and Electromagnetics Laboratory, UIUC, Urbana, IL, USA. From January 2007 to August 2009, he was a Research Fellow with the Radiation Laboratory, University of Michigan, Ann Arbor, MI, USA. Since August 2009, he has been with the King Abdullah University of Science and Technology (KAUST), Thuwal, Saudi Arabia, where he is currently an Associate Professor in electrical and computer engineering. His research interests include various aspects of theoretical and applied computational electromagnetics, with an emphasis on well-conditioned frequency and time domain integral equation formulations and their discretization, hybrid time domain integral and differential equation solvers, accurate, stable, efficient marching schemes for time domain solvers, stochastic characterization of electromagnetic field and wave interactions on complex geometries, and solution of two and three dimensional electromagnetic inverse scattering problem using signal processing techniques. He has authored or co-authored around 130 journal articles and 300 contributions in conference proceedings.

Dr. Bagci is a Senior Member of the URSI Commission B and a fellow of the Applied Computational Electromagnetics Society (ACES). He was a recipient of the 2008 International Union of Radio Scientists (URSI) Young Scientist Award presented at the XXIXth URSI General Assembly and the (2004–2005) Interdisciplinary Graduate Fellowship from the Computational Science and Engineering Department, UIUC, Urbana, IL, USA. His article titled "Fast and Rigorous Analysis of EMC/EMI Phenomena on Electrically Large and Complex Structures Loaded With Coaxial Cables" was one of the three finalists (with honorable mention) for the 2008 Richard B. Schulz Best Transactions Paper Award given by the IEEE Electromagnetic Compatibility Society. He has authored (as student) or co-authored (as a student and an advisor) 19 finalist/honorable mention papers in the student paper competitions at the 2005, 2008, 2010, 2014, 2015, 2016, 2017, 2018, 2020, and 2023 IEEE Antennas and Propagation Society International Symposiums and 2013, 2014, 2016, 2017, 2018, and 2019 Applied Computational Electromagnetics Society Conferences. In 2020, he was one of the recipients of the Gauss Center for Supercomputing (GSC) Award for the paper titled "Solving Acoustic Boundary Integral Equations Using High Performance Tile Low-Rank LU Factorization" and presented at the International Supercomputing Conference (ISC) High Performance. In 2021, he received the KAUST Distinguished Teaching Award, Thuwal, Saudi Arabia. He is currently an Associate Editor of IEEE TRANSACTIONS ON ANTENNAS AND PROPAGATION, IEEE JOURNAL ON MULTISCALE AND MULTIPHYSICS COMPUTATIONAL TECHNIQUES, and *IEEE Antennas and Propagation Magazine*. He has organized and chaired many sessions at IEEE Antennas and Propagation Society International Symposiums and Applied Computational Electromagnetics Society Conferences. Additionally, he served as a Vice Chair (responsible for Computational Electromagnetics Track) of the Technical Program Committee for the IEEE Antennas and Propagation Society International Symposium that was held in Atlanta, GA, USA, in July 2019.